RESEARCH ARTICLE | MARCH 05 2024

# Scaling of drag reduction and logarithmic profile in the turbulent boundary layer over micro-grated superhydrophobic surfaces

Bingfu Zhang (张炳夫) ; Feng Guo (郭枫) ; Suet To (杜雪); Hui Tang (唐辉)



*Physics of Fluids* 36, 035110 (2024)
https://doi.org/10.1063/5.0187893

Physics of Fluids ARTICLE pubs.aip.org/aip/pof

# Scaling of drag reduction and logarithmic profile in the turbulent boundary layer over micro-grated superhydrophobic surfaces

Cite as: Phys. Fluids **36**, 035110 (2024); doi: 10.1063/5.0187893
Submitted: 17 November 2023 · Accepted: 9 February 2024 ·
Published Online: 5 March 2024

View Online Export Citation CrossMark

Bingfu Zhang (张炳夫),[1,a)] Feng Guo (郭枫),[2] Suet To (杜雪),[2] and Hui Tang (唐辉)[3,a)]

## AFFILIATIONS

[1]School of Mechanical Engineering and Automation, Harbin Institute of Technology, Shenzhen, China
[2]State Key Laboratory of Ultra-precision Machining Technology, Department of Industrial and Systems Engineering, The Hong Kong Polytechnic University, Hong Kong, China
[3]Department of Mechanical Engineering, The Hong Kong Polytechnic University, Hong Kong, China

[a)]**Authors to whom correspondence should be addressed:** zhangbfu@hit.edu.cn and h.tang@polyu.edu.hk

## ABSTRACT

We developed a dedicated, high-resolution skin-friction balance in a water tunnel to measure turbulent drag reduction over micro-grate-patterned superhydrophobic (SHPO) surfaces at the Reynolds number $Re_L$ ranging from $4.1 \times 10^5$ to $6.9 \times 10^5$ and achieved a significant drag reduction of up to 46%. The correlation between drag reduction and surface topology was investigated. By considering air fraction, micro-grate gap, and meniscus curvature, an empirical scaling for drag reduction was proposed, which reconciles the widely scattered drag reduction data in the literature. This scaling law could provide a valuable guidance on future design of effective SHPO surfaces for real-world applications. The scaling of the logarithmic layer was also analyzed under the condition that the outer layer has not fully adapted to the SHPO wall manipulation, a common occurrence in experiments due to the limited length of fabricated SHPO surfaces. The slope of the logarithmic layer was found to increase with the drag reduction. Moreover, a theoretical expression describing the slope and up-shifting level of the logarithmic profile was proposed. These results are insightful, providing a new perspective for researchers to examine their velocity profile and drag reduction data in turbulent boundary layers.





## I. INTRODUCTION

Scientists and engineers have taken continuous efforts in past decades to develop techniques for reducing skin-friction drag in multifarious fields of engineering, such as pipelines, ships, underwater vehicles, and micro-fluidic devices. Recent active drag reduction studies using plasma actuations,[1] periodic slit blowing,[2] spanwise wall oscillation,[3] and surface perturbation via piezoelectric actuators[4] have achieved a great success. From the practical point of view, the passive means by surface modification may be more appealing since it requires no gas supply or energy input.[5] One of the most attractive techniques is the use of superhydrophobic (SHPO) surfaces,[6,7] which are obtained by fabricating micro-/nano-textures on a substrate surface.[8] When the SHPO surface is submerged in water flow, air pockets can be entrapped inside the micro-grooves,[9,10] forming plastrons that prevent direct fluid-solid contact and, hence, leading to drag reduction. This technique has received increasing attention with various surface patterns being investigated, including grates,[11–13] posts or cones,[14–16] triangular grooves,[17–19] and random surface structures.[20–23] Moreover, some approaches have been developed to enhance the stability of plastrons on the SHPO surfaces.[7] Examples include hierarchical or reentrant structures,[24–26] chemical or electrochemical air regeneration,[27,28] air bubble injection,[29,30] and surface plastron replenishment.[31]

For laminar boundary layers, it has been well established that the drag reduction mechanism of SHPO surfaces is primarily due to the liquid slipping over the shear-free liquid–air interface,[32,33] whereas for turbulent boundary layers (TBL), drag reduction is due to the combined effect of the slipping and the attenuation of turbulent flow structures.[34,35] Among different surface topologies such as random roughness, posts, and grates, the streamwise-aligned grate is perhaps the most effective in reducing skin-friction drag.[11–13] Table I summarizes existing experimental studies using streamwise micro-grates in water channels/tunnels, towing tanks, and open water. In a channel flow with SHPO surfaces, Daniello *et al.*[36] obtained, based on particle image velocimetry (PIV) measurements, a maximum drag reduction

**TABLE I.** Summary of experimental studies on turbulent drag reduction using streamwise-micro-grated SHPO surfaces. Note: The friction Reynolds number $Re_\tau$ is calculated by $u_\tau H/2\nu$ and $u_\tau \delta_B/\nu$ for the channel flow and TBL, respectively, where $u_\tau$ is friction velocity, $\nu$ is kinematic viscosity, $H$ is the channel height, and $\delta_B$ is boundary layer thickness. FSD denotes the friction measurement based on detecting the floating surface displacement under shear stress. The $DR_{max}$ denotes the achieved maximum drag reduction.

| Researchers | Flow type | $Re_\tau$ | $f_a$ | $g_0^+$ | Measurement | $DR_{max}$ |
|---|---|---|---|---|---|---|
| Daniello *et al.*[36] | Channel flow | 110–260 | 50% | 0.8–2 | PIV | 25% |
| Woolford *et al.*[37] | Channel flow | 100–160 | 80% | 1.3–2.2 | PIV | 11% |
| Park *et al.*[11] | Water tunnel | 250 | 30%–95% | 0.3–1.9 | FSD | 75% |
| Xu *et al.*[12] | Open water | 2000–6000 | 90% | 5–30 | FSD | 38% |
| Xu *et al.*[13] | Towing tank | 2000–6000 | 90% | 3.2–9.3 | FSD | 27% |

of approximately $DR = 27\%$ with an air fraction $f_a = 50\%$ (here, $DR$ is defined as the ratio of the drag decrease using SHPO surfaces to the drag of a baseline smooth surface under the same flow condition. $f_a = g/p$ is defined as the ratio of the air–water interface area to the overall projected area of the SHPO surface, where $g$ and $p$ are the gap and pitch between two neighboring grates, respectively). However, using a much larger air fraction of $f_a = 80\%$, Woolford *et al.*[37] only achieved a $DR$ of 11%. In a water-tunnel experiment with $f_a = 95\%$, Park *et al.*[11] attained a much larger $DR$ of 75%. However, in Xu *et al.*'s[13] towing-tank tests, the obtained $DR$ was only 27%, albeit with a comparable $f_a$ of 90%.

The dependence of turbulent drag reduction on the topology of micro-grated SHPO surfaces has also been studied. Daniello *et al.*[36] experimentally investigated the effect of $g_0^+$ on $DR$ in a channel flow at the Reynolds number $Re_H$, based on the channel height and the mean flow velocity, ranging from 3000 to 9500 (in this paper, the superscript "$^+$" indicates normalization by the friction velocity $u_\tau$ and/or the viscous length scale $\delta_v$, and the subscript "$_0$" denotes quantities measured over the baseline smooth surface). They found that $DR$ initially grew with $g_0^+$ and then was saturated at about 27% when $g_0^+$ exceeded 1.2. However, Xu *et al.*[13] observed in towing-tank experiments a continuous rise in $DR$ from 18% to 27% with $g_0^+$ increasing from 4 to 10. In their open-water test using a SHPO surface with $g = 90$ and $p = 100\ \mu$m, Xu *et al.*[12] found that $DR$ retained nearly unchanged at about 30% at $g_0^+$ ranging from 12 to 25. However, there are very few experimental studies on the effect of $f_a$ on the drag reduction.[2] Regarding the effect of $f_a$, Park *et al.*[11] experimentally indicated an exponential increase in $DR$ from 3% to 75% with $f_a$ increasing from 30% to 75%. However, this differs from the approximately linear relationship as observed in Park *et al.*'s[38] numerical study.

Past studies[7,39] have identified two important geometrical parameters governing the drag reduction, i.e., $f_a$ and $g_0^+$. Nevertheless, the reported dependence of $DR$ on $f_a$ and $g_0^+$ varies greatly.[7] For instance, Refs. 11, 13, 36, and 37, as revealed in Table I, $DR$ scatters between 14% and 30% given nearly the same parameters of $f_a \approx 50\%$ and $g_0^+ \approx 1$, and between 11% and 65% for $f_a \approx 90\%$ and $g_0^+ \approx 2$. Such large variations cannot be simply ascribed to the differences in experimental conditions such as measurement settings, Reynolds number and possible loss of plastron on their SHPO surfaces. Some questions are, therefore, raised: Is using $f_a$ and $g_0^+$ adequate to achieve a good correlation between the drag reduction and the surface topology? Are there any other factors, such as the water pressure on SHPO surfaces and the resultant deformation of the air–water interface, that should be taken into consideration? Furthermore, could we obtain a scaling law that can deduce drag reduction from flow conditions and surface topologies?

In addition to drag reduction, numerous experimental and numerical investigations on TBL over SHPO surfaces have also revealed an upward shift of the mean velocity profile from that over a smooth surface.[14,15,29,35] In most of these studies, the slope of the up-shifted velocity profile in the logarithmic layer over the SHPO surface, scaled by its own inner units, was assumed unchanged. For instance, in their direct numerical simulation (DNS) study on the logarithmic layer scaling over micro-grated SHPO surfaces, Martell *et al.*[14] claimed that the logarithmic profile was characterized by the same slope as that over the smooth surface, but was offset by the magnitude of the slip velocity $U_s^+$. In Zhang *et al.*'s[40] and Li *et al.*'s[35] water-tunnel experiments using SHPO surfaces with random roughness, they stated that the slope of the lifted logarithmic profile over the SHPO surface retained unchanged from that over the smooth surface, and the offset of the logarithmic profile may be affected by the magnitude of $DR$. However, this assumption may be questionable if the longitudinal length of SHPO surface is not sufficiently large, so that the outer layer has not reached a new equilibrium with the wall manipulation. This is supported by Ling *et al.*'s[21] water-tunnel study on drag reduction using randomly textured SHPO surfaces based on high-resolution PIV measurements, in which a substantial $DR$ of 27% was achieved. It was observed that, at a downstream location of approximately 13 times boundary layer thickness from the beginning of the SHPO surface, the profiles of viscous shear stress over the baseline smooth and the SHPO surfaces collapsed in the outer layer. They, therefore, presumed that this non-equilibrium condition may influence the slope of the logarithmic profile.

Nevertheless, there are very few experimental or numerical studies in which the SHPO surface is documented to be long enough to capture the equilibrium condition, and the relationship between the slope of the logarithmic profile and the drag reduction has yet to be established. Therefore, this work sets out to address this issue by obtaining a theoretical expression describing the logarithmic profile scaling over SHPO surfaces. The findings from the present study could be important in two aspects. First, research groups working on the drag reduction of SHPO surfaces can compare their velocity data with our proposed theory and evaluate to what extent the outer layer has been affected by the wall manipulation. Second, fitting the logarithmic profile has been a widely used method in estimating the drag reduction of SHPO surfaces,[29,40,41] and hence, the present results are valuable for researchers to predict drag reduction from their logarithmic profile data.

To facilitate the present study, an in-house, high-resolution skin-friction balance is developed for direct measurement of small TBL drag reductions over streamwise-micro-grated SHPO surfaces, such that reasonably accurate data can be obtained for the validation of relevant theoretical models and numerical simulations. Experimental details are given in Sec. II. The results are presented in Sec. III, including the baseline flow characteristics, the drag reductions and associated scaling law of SHPO surfaces, along with the analysis on the logarithmic scaling changes. This work is concluded in Sec. IV.

## II. EXPERIMENTAL DETAILS

### A. SHPO surface fabrication

The SHPO surface was textured with an array of micro-grates on an $80 \times 80 \times 7\,\text{mm}^3$ flat cyclic olefin copolymer (Topas COC 8007S-04) sheet using the ultra-precision machining technique. This streamwise length (80 mm) is four times that (20 mm) used in Park *et al.*[11] and appreciably longer than that (70 mm) in Xu *et al.*[13] Plastic injection molding was used to prepare the COC sheet. Then, single-point diamond turning using a Nanoform 200 machine was employed to cut the surface at the same level. After this process, the surface roughness was measured to be within 1 $\mu$m. A Moore Nanotech 350FG 4-axis Ultra-precision Machine was applied to fabricate micro-grates on the flat sheet. A single crystal diamond facet cutting tool was used in the machining process. Different tool tip widths ($w_t$), ranging from 10 to 30 $\mu$m, were utilized in fabricating different micro-grate geometries. The unidirectional retreat method was deployed to generate the micro-grated surface by tool path planning, as illustrated in Fig. 1(a). The grate cutting was launched at the start point, and advanced spanning the surface along the grate direction, i.e., the feed direction. Then, the cutting tool retreated to the start point, but shifted perpendicularly to the feed direction, referred to as the raster direction, in which the shift distance was determined by the designed grate spacing. After that, the next cycle of grate machining started. Four steps of cutting, with each step at a specific value of cutting depth, were employed in generating the grates on the whole surface [Fig. 1(b)]. The depth of the first three cutting steps was 12 $\mu$m and that of the finish-cut was 6.3 $\mu$m. After generating the grates, horizontal cutting with a depth of 5 $\mu$m was performed at the top of the ridges to ensure a flat top surface.

There are a relatively small number of experimental studies on turbulent drag reduction using micro-grated SHPO surfaces,[11–13,36,37] which is probably due to the difficulty in fabricating organized surface structures. In most of these studies, the micro-grated SHPO surfaces were fabricated using the conventional photolithography technique. However, this approach is normally associated with long

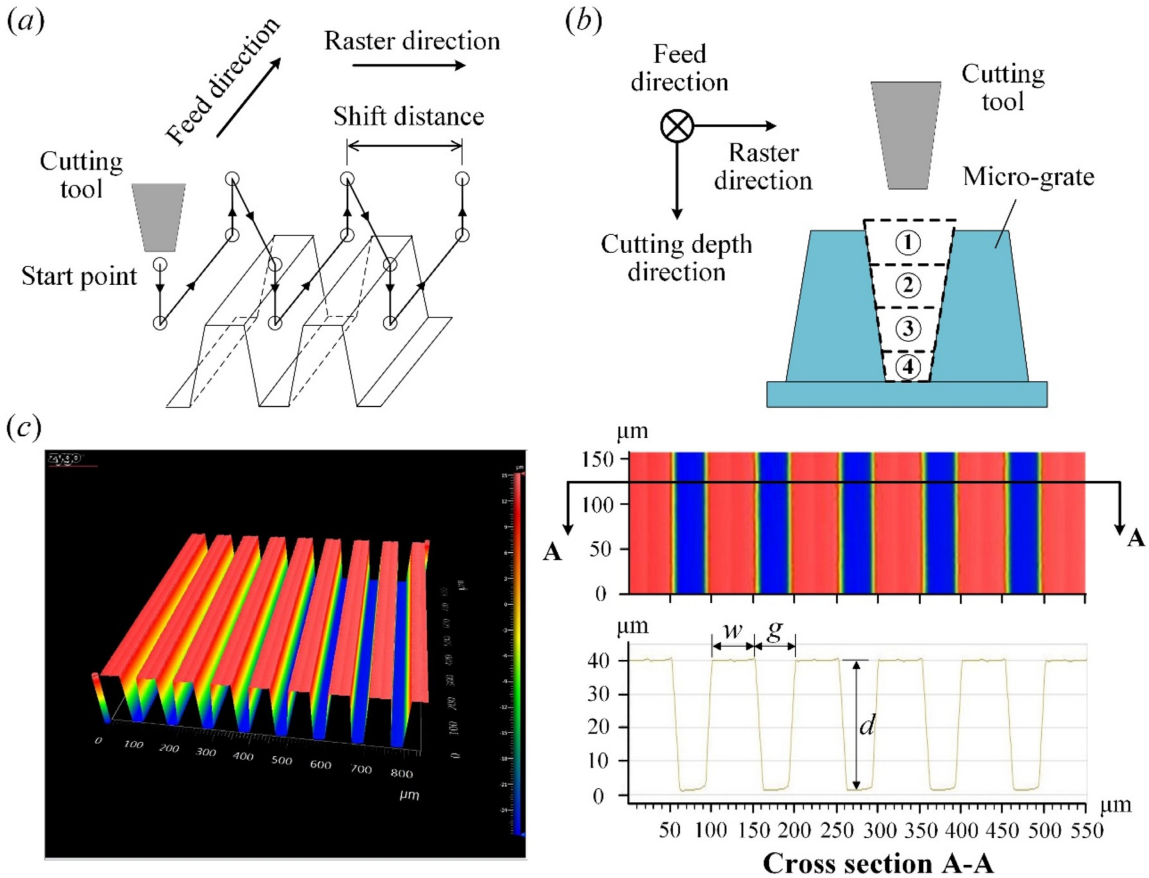


**FIG. 1.** (a) Schematic of cutting tool path design of fabricating the micro-grated surface. (b) Cutting steps in the cutting strategy. (c) White light interferometer image of the SHPO$^{\#2}$ surface topology.

**TABLE II.** Geometrical parameters of the four SHPO surfaces.

| Surface samples | $p$ ($\mu$m) | $w$ ($\mu$m) | $g$ ($\mu$m) | $f_a$ | $d$ ($\mu$m) |
|---|---|---|---|---|---|
| SHPO$^{\#1}$ | 60 | 30 | 30 | 50% | 37 |
| SHPO$^{\#2}$ | 100 | 50 | 50 | 50% | 37 |
| SHPO$^{\#3}$ | 60 | 40 | 20 | 33% | 37 |
| SHPO$^{\#4}$ | 100 | 70 | 30 | 30% | 37 |

manufacturing duration, complexity of its realization, and only suitable to the materials related to silicon. In the present study, the micro-grates on SHPO surfaces were fabricated using the ultra-precision machining technique, which requires no complex chemical reaction and can be applied to various materials including plastics, semiconductors, ceramics, and optical glasses. By changing the size of the single crystal diamond facet cutting tool and the tool path planning, as illustrated in Fig. 1, different micro-grate geometries can be manufactured and with a relatively high form accuracy of approximately 1 $\mu$m.

The selection of micro-grate geometries is based on the following considerations. In their water-channel experiments using a micro-grated SHPO surface with $p = 60$ and $g = 30\,\mu$m, Daniello *et al.*[36] observed based on PIV measurements that *DR* initially climbed rapidly from 10% to 27% when $g_0^+$ was increased from 0.8 to 1.2. Beyond $g_0^+ = 1.2$, there was nearly no further improvement in *DR*. This observation suggests that $g_0^+$ should at least approach 1.2 in order to achieve a tangible drag reduction. In the present study, the smooth surface viscous length $\delta_{v0}$ was measured to be from 39.1 to 63.1 $\mu$m at the tested Reynolds number $Re_L$ ranging in (4.1–6.9) $\times$ $10^5$. As such, $g_0^+ = 1.2$ corresponds to $g = 46.9$–$75.7\,\mu$m. Nevertheless, an excessively large $g$ may impair the stability of the air–water interface and cause an easy escape of air.[7] Indeed, in present water-tunnel tests, it was observed that, if $g$ exceeded 70 $\mu$m, the plastron on the SHPO surface depleted relatively quickly within about 10 min. Thus, three different $g$ values, i.e., 20, 30, and 50 $\mu$m were selected, with the air fraction $f_a$ ranging from 30% to 50%. Four different SHPO surface samples were manufactured, denoted as SHPO$^{\#1}$, SHPO$^{\#2}$, SHPO$^{\#3}$, and SHPO$^{\#4}$, with pitches of $p = 60$, 100, 60, and 100 $\mu$m, grate top widths of $w = 30$, 50, 40, and 70 $\mu$m, resulting in air fractions of $f_a = (p - w)/p = 50\%$, 50%, 33%, and 30%, respectively. The grate heights $d$ of the four surface samples are fixed at 37 $\mu$m. Table II summarizes the geometrical parameters for these SHPO surfaces. The topology of surface structures of one typical surface sample (SHPO$^{\#2}$) measured by a white light interferometer (Zygo Nexview) is shown in Fig. 1(c), presenting sharp top edges of the micro-grate. In addition, a smooth surface of the same size was made using the same material, serving as the baseline surface for comparison purposes. Measurements of the contact angles on these surfaces revealed that the smooth surface has a static contact angle of 94°, whereas the four SHPO surfaces have almost the same static contact angle of 152°, indicating good hydrophobic properties.

## B. Experimental setup

### 1. Friction drag measurements

Experiments were conducted in a closed-loop water tunnel with a test section of 2.4 m (length) $\times$ 0.3 m (width) $\times$ 0.6 m (height). Two optical glass windows of 0.86 m (length) $\times$ 0.4 m (height) $\times$ 0.03 m (thickness), aligned one behind the other in the streamwise direction, were embedded in the water tunnel sidewall to facilitate optical observations and measurements. Drag reduction tests were performed at water flow velocity $U_\infty = 0.33$–$0.55$ m/s. Within this $U_\infty$ range, the non-uniformity of the streamwise velocity was about 0.1%, and the freestream streamwise turbulence intensity was less than 1.2%.

Figure 2 schematically illustrates the experimental setup. A flat plate of 1.8 m (length) $\times$ 0.29 m (width) $\times$ 0.02 m (thickness) was suspended horizontally in the test section by a ground-fixed rigid frame. The leading edge of the plate was made a clipper-built curve to

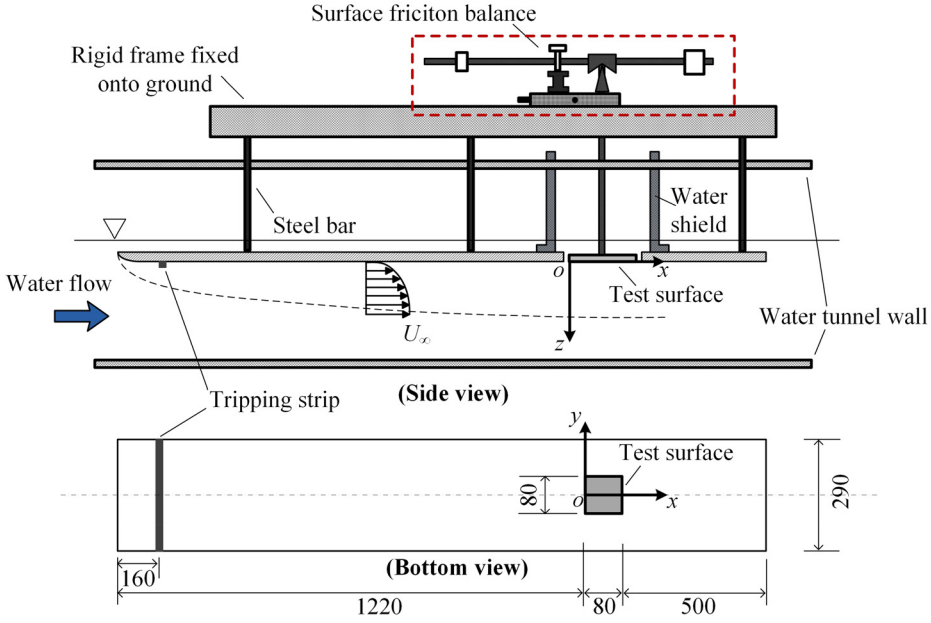


**FIG. 2.** Schematic of experimental setup in water tunnel test section. The length unit is mm.

minimize flow separation. Two arrays of cylindrical roughness elements arranged in the spanwise direction were placed 0.16 m downstream from the plate's leading edge to trip the boundary layer into turbulence. A square hole of $80.4 \times 80.4\,\text{mm}^2$ was cut in the plate to accommodate the test surfaces, with its center located 1.26 m downstream from the plate's leading edge. The Reynolds number $Re_L$ (based on the distance from the plate's leading edge to the center of test surface) ranges from $4.1 \times 10^5$ to $6.9 \times 10^5$, corresponding to $Re_{\tau 0}$ (based on $u_{\tau 0}$ and $\delta_{B0}$) from 560 to 810. The water level was kept 40 mm above the lower surface of the flat plate throughout the tests. A right-handed Cartesian coordinate system ($x$, $y$, $z$) is defined as shown in Fig. 2, with its origin $o$ located at the middle of the leading edge of the test surface, the $x$ axis along the freestream direction, and the $z$ axis pointing downward.

The drag on the SHPO surface was directly measured using an in-house, high-resolution skin-friction balance [Fig. 3(a)], which has been successfully deployed in a wind tunnel for surface friction measurement.[42] In contrast, the commonly used indirect measurement method by evaluating the skin friction from the PIV-measured velocity profiles usually suffers from limited spatial resolution and laser reflection on walls.[43] The working principle of this balance is depicted in Fig. 3(b). A vertical frame sat on a pair of knife edges which were mounted on a ground-fixed rigid frame to preclude the influence of tunnel vibration on the measurements. The vertical frame was enclosed in a sealed compartment, and thereby it was not subject to any hydrodynamic force. The test surface was installed at the lower end of the vertical frame and placed right in the square hole of the plate, flush with the plate's lower surface. The gap between each edge of the test surface and the respective edge of the square hole was approximately 0.2 mm. The upper end of the vertical frame was connected with a horizontal bar. A sliding block, which sat on the horizontal bar, connected with a load cell (ATI Nano43) through an adjustable vertical rod, and thereby the horizontal arm $l_h$ (i.e., the horizontal distance between the knife edges and the sliding block) can be adjusted. In this study, the ratio of the horizontal arm $l_h$ to the vertical arm $l_v$ (i.e., the vertical distance between the knife edges and the test surface) was fixed at 10.5, defining a gain factor by which the load-cell readings are amplified. To preload the load cell in its normal working range, two balancing weights were used. With this balance, the skin-friction drag on the test surface is determined by $F_D = F_z l_h / l_v$, where $F_z$ is the force read by the load cell. The friction drag coefficient is evaluated by $C_f = 2F_D/\rho U_\infty^2 A$, where $\rho$ is the water density and $A$ is the surface area. The drag reduction is then quantified using the normalized change in drag coefficient, i.e., $DR = (C_{f0} - C_f)/C_{f0}$. Since the load cell has a sensitivity of about $10^{-4}$ N, and reads loads (i.e., the skin-friction drag magnified through the gain factor) of the order $10^{-2}$ N, its measurement resolution is approximately 1%.

The skin-friction balance was calibrated *in situ* after mounting the test surfaces in the water tunnel. A calibrating device was built to produce a small well-defined force [Fig. 4(a)]. Operating on a similar principle as the balance, this device consists of a knife edge, horizontal and vertical bars, and a hook on the horizontal bar to attach calibrated loads. As such, when a downward load $G_{in}$ was applied to the hook at the position W, it was translated to a load $G_{out}$ exerting on the test surface in the direction parallel to the surface. Its magnitude can be calculated by $G_{in} \cdot l_p / l_n$, where $l_p$ and $l_n$ are the arms for $G_{in}$ and $G_{out}$, respectively. The deflection of the test surface under $G_{out}$ was negligible, and therefore, the arms of the balance ($l_v$ and $l_h$) and of the calibrating device ($l_p$ and $l_n$) retained the same throughout the calibration process. Figure 4(b) displays the calibration curve of the balance, which shows perfect linearity between the output loads read from the balance and the input loads. The slope of the fit line determined from the least squares fitting is about 10.5, equaling the pre-set gain factor of the balance. The root mean square (RMS) of deviations of the output data from the fitted line is very small, only approximately 0.04 g, which is less than 0.1% of the full output load. Before each test run, which requires a separate assembly of the test setup, the skin-friction balance was calibrated. The calibration was performed before filling the water tunnel, after which the measurement was carried out.

Since the force signal from the load cell was sensitive to ambient temperature, the room temperature was maintained at 296 K throughout the experiments using air conditioners in the laboratory. After switching on the air conditioners and setting the control panel, the room temperature will reach this temperature and maintain stable after about 1 h. During the tests, one thermometer was also used to monitor the room temperature. The load cell signal was acquired at a sampling frequency of 1 kHz with four steps. First, signal recording was initiated before starting the water flow ($U_\infty = 0$). In this step, the sampling duration was 20 s, and the acquired data were averaged and referred to as the baseline load cell signal. Second, with the data

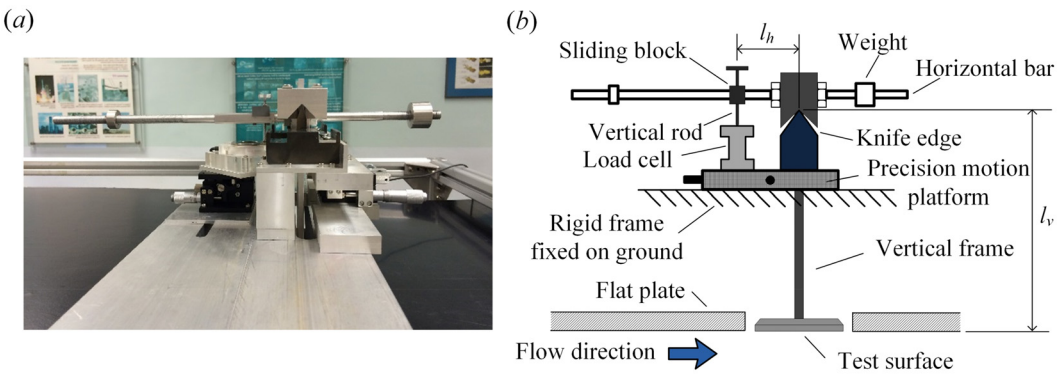


**FIG. 3.** (a) Photograph of the skin-friction balance in water tunnel tests. (b) Illustration of the friction balance system.

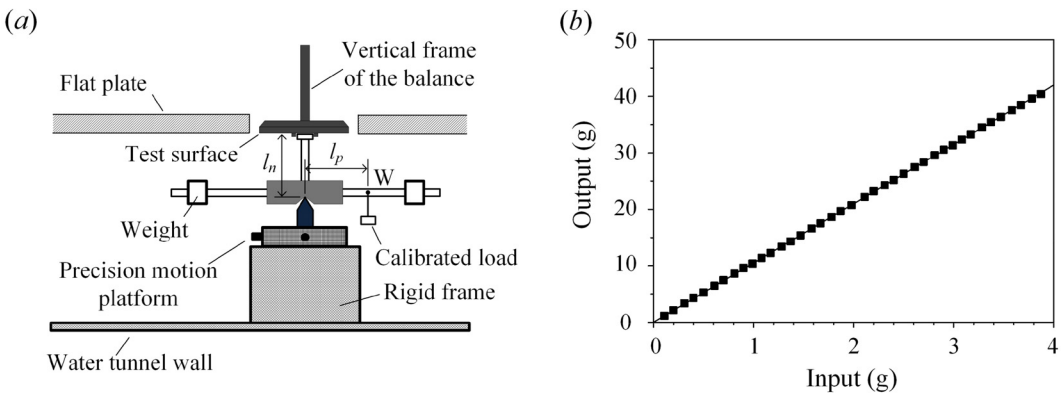


**FIG. 4.** (a) Schematic of the calibration device. (b) The calibration curve of the balance. The solid line is the least squares fit to the measured output over input range from 1 to 4 g.

acquisition continuing, the water tunnel pump was switched on to obtain the desired $U_\infty$. This step was normally completed in 60 s. After that, the $U_\infty$ was maintained at the steady state for an additional 100 s, resulting in a cumulative signal sampling time of 180 s. The data acquired in the last 20 s in this step were averaged and denoted as the load cell signal under this particular $U_\infty$. Then, the friction drag was calculated based on $F_z$, which was determined by the change in the load cell signal from the baseline. Finally, the water speed was decreased to zero, which took about 200 s. Data acquisition was performed in the still water for 20 s, and the acquired data were compared with the baseline signal to make sure the data were consistent throughout the test. At least three testing runs were performed for each test configuration.

The air layer over SHPO surfaces was monitored using a camera to ensure that the plastron remained complete on the SHPO surfaces during the measurements. A light-emitting diode (LED) beam generated from a 10 W white LED light source was used outside the tunnel. The centerline of the beam was fixed in the ($y$, $z$) plane at $x = 0$ with an incidence angle of 45°. The beam was reflected at the air–water interface, and then captured by the camera placed beneath the transparent water-tunnel bottom wall, resulting in bright strips in the captured photographs. As shown in Figs. 5(a) and 5(b), the air plastron on the SHPO$^{\#1}$ surface is characterized by the region with a bright color, in contrast with the case when the surface is fully wetted and the bright region disappears [Fig. 5(c)]. The close-up in Fig. 5(b) clearly shows longitudinally aligned silver stipes, which are apparently associated with the air pocket trapped inside the grates. Similar observations have also been made for the other three SHPO surfaces. The plastron was observed to retain intact for at least 20 min in all the drag reduction test cases, longer than needed (about 5 min) to complete the tests.

It is worth mentioning that, when the SHPO surfaces are submerged in water flow during the tests, the micro-grates are rigid enough to avoid structural deformation or elimination when subjected to wall shear stress. Moreover, there is nearly no dissolution or chemical reaction for the COC material in water. The structural stability of the micro-grates has also been verified based on microscope measurements after each test, in which the micro-grate geometry was observed to remain unchanged.

### 2. PIV measurements

A Dantec two-dimensional time-resolved PIV system was used to measure the boundary layer in the $y = 0$ plane. The flow was seeded with Dantec Dynamics polyamide seeding particles with a mean diameter of 5 $\mu$m. Flow illumination was provided by a ReyPower 10 W continuous laser source of 532 nm in wavelength. The laser sheet was about 1 mm thick. A high-speed camera (Photron FastCam UX100, with a resolution of 1280 × 1024 pixels) with a Micro-Nikkor 200 mm lens was used to capture particle images. At $U_\infty = 0.33$ m/s, the PIV image covered an area of $x_0^+ = 492$–$1078$ and $z_0^+ = 0$–$713$. The image magnifications in both directions of this ($x$, $z$) plane were identical, about 39 $\mu$m/pixel. The images were captured in single-frame mode at a frequency of 1 kHz, leading to a time separation of 1 ms, during which the seeding particles may travel a distance of 0.33 mm, corresponding to about 9 pixels. In processing PIV images, the adaptive PIV method (Dynamic Studio software) was used with a minimum interrogation area size of 16 × 16 pixels and a maximum size of 32 × 32 pixels, and the grid step size of 8 × 8 pixels, producing 118 × 144 in-plane velocity vectors with a spacing of 0.29 mm (about $4.6\delta_{v0}$). The instantaneous velocity components in the $x$ and $z$ directions are designated as $U$ and $V$, which can be decomposed as $U = \overline{U} + u$ and $V = \overline{V} + v$, respectively, where the overbar denotes time-averaging, and $u$ and $v$ are the fluctuating velocity components. A total of 4000 images were captured for each case.

Following Refs. 44–47, a method based on image matching analysis was used to determine the PIV measurement uncertainty. This approach identifies particle image pairs in two successive exposures according to the measured displacement vectors and evaluates the residual distance or particle disparity between the particle image pairs, which dictates the uncertainty of velocity measurements. Further details of this technique can be found in Sciacchitano *et al.*[47] The seeding densities in the captured PIV images were about ten particles per interrogation window. The RMS value of the disparity was found, based on the Dynamic Studio software, to be about 0.1 pixel in both $x$ and $z$ directions, resulting in the uncertainties, $\varepsilon_U$ and $\varepsilon_W$, in $U$ and $W$ of 1%$U_\infty$, respectively. It has been confirmed that the region affected by the laser light reflection in the captured images was within a distance of $\lambda \approx 0.5$ mm or $\lambda_0^+ \approx 8$ from the test surface. The affected

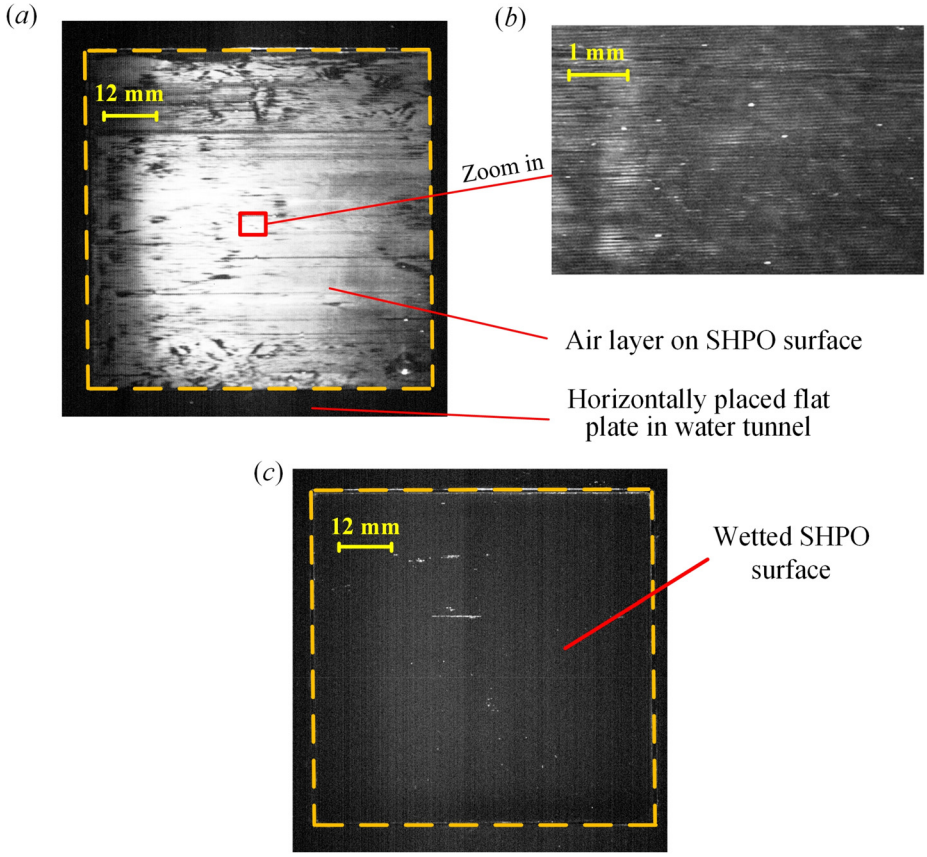


**FIG. 5.** Photographs of (a) plastron on the SHPO$^{\#1}$ surface and (c) fully wetted SHPO$^{\#1}$ surface. (b) is a zoom of (a) in the central region of the surface. The flow is from left to right at $Re_L = 4.1 \times 10^5$.

region was masked with a black color to eliminate its influence during processing the PIV images.[48]

## III. RESULTS AND DISCUSSION

Drag reductions of the four SHPO surface samples are investigated based on skin-friction balance measurements, with which an empirical scaling is proposed. Then, the scaling of PIV-measured mean velocity profiles on these surfaces is discussed.

### A. Drag reduction of SHPO surfaces

Figure 6 compares the measured friction drag coefficients and drag reductions for the smooth and four SHPO surfaces at $Re_{\tau 0}$ from 560 to 810 ($Re_L$ from $4.1 \times 10^5$ to $6.9 \times 10^5$). The resulting TBL characteristic parameters at a selected Reynolds number $Re_L = 4.1 \times 10^5$ are listed in Table III, including $\delta_B$, $\delta_\nu$, $u_\tau$, $C_f$, and wall shear stress $\tau_w$. The friction drag on the smooth surface is first examined to assess the accuracy of the skin-friction balance tests. $C_{f0}$ exhibits a slight decrease from 0.0047 to 0.0044 as $Re_L$ increases from $4.1 \times 10^5$ to $6.9 \times 10^5$ [Fig. 6(a)]. The measured drag coefficient is also compared with the empirical correlation for TBL suggested by White,[49] i.e.,

$$C_{f0} = \frac{0.455}{\ln^2(0.06Re_x)}, \tag{3.1}$$

where $Re_x$ is the Reynolds number based on the distance from the leading edge of the plate. Here, we approximate $Re_x$ by $Re_L$ in estimating $C_{f0}$ since the length of the test surface (0.08 m) is only about 6% of $L_c$. It can be seen that the measured drag and its variation agree well with the prediction by Eq. (3.1). The deviation of the measured data from the prediction is approximately 2%–6% for different $Re_L$. The error bars shown in Fig. 6(a) describe the uncertainty of drag coefficients, defined as $\overline{\left|C_{f0} - \overline{C_{f0}}\right|}$, where the double overbar denotes the average over three independent test runs,[44,45,50] and is estimated to be between 2.3% and 5.1%.

All the four SHPO surfaces can significantly reduce the skin-friction drag, though the extent of drag reduction varies [Fig. 6(b)]. The SHPO$^{\#1}$ surface generates the largest $DR$, from 41% to 46% as $Re_{\tau 0}$ increases from 560 to 810. The trend of variation in $DR$ is consistent with Xu *et al.*'s[13] observation in towing-tank experiments using a micro-grated SHPO surface with $f_a = 90\%$. They found that $DR$ increased from 19% to 27% at $Re_{\tau 0}$ from 2500 to 4400, and ascribed the $DR$ increase to the growing $g_0^+$ from 5 to 10. It is, therefore, plausible that the growing $DR$ with $Re_{\tau 0}$ for the SHPO$^{\#1}$ surface may be connected to the increased $g_0^+$, which varies from 0.5 to 0.8. It is worth mentioning that the currently obtained drag reductions fall in the upper range of values reported in the literature in TBL flows,[7,39] supporting that streamwise micro-grates may be more effective in reducing the friction drag as compared with other surface topologies.[13] For instance, Henoch *et al.*[51] achieved a maximum $DR$ of about 20% with a micro-post-patterned surface. Other studies using random structures obtained maximum $DR$ ranging from 10% to 36%.[21,35,40,52]

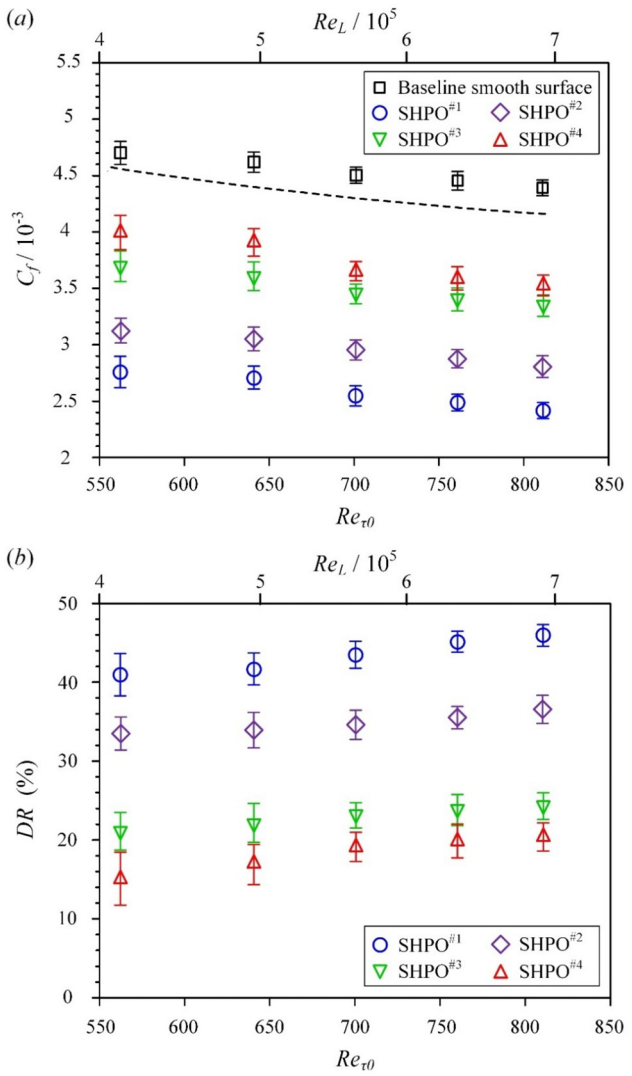


**FIG. 6.** Dependence of (a) $C_f$ and (b) $DR$ on $Re_\tau$ and $Re_L$ for the test surfaces. The uncertainty bars of $C_f$ and $DR$ are given by $\overline{|C_f - \overline{C_f}|}$ and $\overline{|C_f - \overline{C_f}|}/\overline{C_{f0}}$, respectively. The dashed line is the prediction from an equation of $C_{f0} = 0.455/\ln^2(0.06Re_L)$ for a smooth surface in TBL.[49]

**TABLE III.** TBL flow parameters over baseline and SHPO surfaces at $U_\infty = 0.33$ m/s ($Re_L = 4.1 \times 10^5$).

| Samples | $\delta_B$ (mm) | $u_\tau$ (m s$^{-1}$) | $\delta_\nu$ ($\mu$m) | $Re_\tau$ | $\tau_w$ (kg m$^{-1}$ s$^{-2}$) | $C_f$ |
|---|---|---|---|---|---|---|
| Smooth | 35.6 | 0.0160 | 63.1 | 564 | 0.256 | 0.0047 |
| SHPO$^{\#1}$ | 37.7 | 0.0122 | 82.5 | 455 | 0.149 | 0.0027 |
| SHPO$^{\#2}$ | 37.3 | 0.0130 | 77.7 | 480 | 0.169 | 0.0031 |
| SHPO$^{\#3}$ | 36.6 | 0.0142 | 71.1 | 515 | 0.202 | 0.0037 |
| SHPO$^{\#4}$ | 36.4 | 0.0148 | 68.4 | 533 | 0.219 | 0.0040 |

With the same air fraction (i.e., $f_a = 50\%$) but a larger grate pitch (increased from $p = 60$ to $100\,\mu$m), the SHPO$^{\#2}$ surface produces appreciably lower $DR$, ranging from 33% to 37%, at the same $Re_{\tau 0}$ range. If $f_a$ further reduces to 30%–33%, SHPO$^{\#3}$ and SHPO$^{\#4}$ surfaces result in relatively moderate $DR$ of 21%–24% and 16%–20%, respectively, which are considerably smaller than those (33%–46%) produced by SHPO$^{\#1}$ and SHPO$^{\#2}$ surfaces.

The shape of air–water interface or meniscus in the grate gap has been found to have an important impact on the drag reduction for both laminar and turbulent flows.[53–55] According to the meniscus deformation analysis by Rastegari and Akhavan,[53] the shape of the interface ($F_p$) in a right-handed coordinate system ($x_p$, $y_p$, $z_p$), with its origin $o_g$ centered on the groove as shown in Fig. 7, may be written as

$$F_p\left(y_p,\ \Delta P\right) = \frac{g}{2k_c}\left(\sqrt{4-k_c^2} - 2\sqrt{1-\left(k_c\, y_p/g\right)^2}\right), \tag{3.2}$$

where $\Delta P$ is the Laplace pressure across the interface, estimated by the static pressure at the surface ($\approx$400 Pa). $k_c = \Delta P\ g/\sigma$ is the non-dimensional curvature of the interface, where $\sigma$ is the surface tension. Then, the protrusion angle ($\theta_p$) and the maximum meniscus bending depth ($h_p$) can be respectively calculated by

$$\theta_p = \arctan\left(\frac{k_c}{\sqrt{1-(k_c/2)^2}}\right) \tag{3.3}$$

and

$$h_p = \frac{g}{2k_c}\left(2-\sqrt{4-k_c^2}\right). \tag{3.4}$$

According to Eqs. (3.3) and (3.4), the $\theta_p$ and $h_p$ values for SHPO$^{\#2}$ are about 15° and 1.7 $\mu$m, respectively, which are higher than those (9° and 0.6 $\mu$m) for SHPO$^{\#1}$. In Rastegari and Akhavan's[53] numerical study on turbulent drag reduction using streamwise micro-grates, they

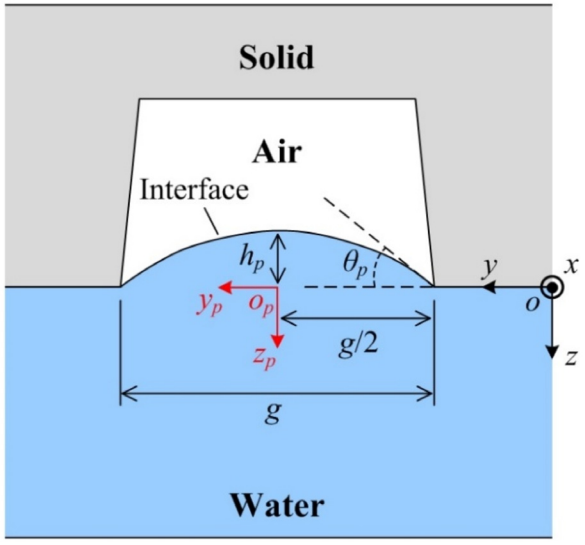


**FIG. 7.** Schematic of the bending air-water interface formed over micro-grates.

found that the slip velocity $U_s$ and the resultant $DR$ were decreased by about 14% and 13%, respectively, as $\theta_p$ increased from 0° to 30°. Moreover, an increase in $h_p$ could lead to a decline in the slip length $b$ and, hence, in the drag reduction.[56] It is, therefore, plausible that the lower $DR$ obtained by SHPO$^{\#2}$ may be associated with the larger deformation of the meniscus.

Figure 8 presents the PIV-measured normalized Reynolds stresses $\langle\overline{uu}\rangle_0^+$ and $\langle\overline{vv}\rangle_0^+$ over the smooth and SHPO$^{\#1}$ surfaces at $Re_L = 6.9 \times 10^6$, where the angular brackets denote quantities spatially averaged in the $x$ direction. The flow over the SHPO$^{\#1}$ surface exhibits lower streamwise velocity fluctuations as compared with the smooth surface [Fig. 8(a)]. At $10 < z_0^+ < 30$ (i.e., the buffer layer), $\langle\overline{uu}\rangle_0^+$ is considerably reduced over the SHPO$^{\#1}$ surface, with its peak value decreased by approximately 16% if compared to that over the smooth surface. The turbulence attenuations also extend to the logarithmic layer until $z_0^+ \approx 60$, albeit with appreciably less prominent reductions. Similar observations can also be made from the $\langle\overline{vv}\rangle_0^+$ profiles as shown in Fig. 8(b), suggesting weakened vertical velocity fluctuations over the SHPO$^{\#1}$ surface. These results agree with the water-tunnel experiments by Zhang *et al.*,[40] Tian *et al.*,[41] and Ling *et al.*[21] using SHPO surfaces with random roughness, where diminished $u$ and $v$ fluctuations in the buffer and logarithmic layers were observed from PIV measurements. Moreover, Park *et al.*[38] numerically investigated the turbulent structures over micro-grated SHPO surfaces and found that the near-wall quasi-streamwise vortices were weakened on the SHPO surface as compared with the smooth surface. This observation is consistent with the study of Zhang *et al.*,[40] in which the PIV-measured vorticity and swirling strength data showed weakened turbulent structures above a randomly textured SHPO surface. Furthermore, Hokmabad and Ghaemi[20] experimentally observed a noticeable suppression of the sweep and ejection events over the SHPO surface and indicated that the turbulence regeneration cycle could be attenuated due to the slip on SHPO surface. It is, therefore, inferred that the reduction in $\langle\overline{uu}\rangle_0^+$ and $\langle\overline{vv}\rangle_0^+$ over the SHPO$^{\#1}$ surface (Fig. 8) may be linked to the weakening of vortical structures and the suppression of turbulent activities, which leads to the significant $DR$ of 46%.

In their DNS study on the mechanism of turbulent drag reduction using micro-grated SHPO surfaces, Rastegari and Akhavan[34] indicated that the drag reduction came mainly from two parts, i.e., one resulted from the slip on the surface and the other from modifications to near-wall turbulent structures. The former was found to contribute more than 80% of the total drag reduction. This result was corroborated by Li *et al.*'s[35] water-tunnel experiments. Based on high-resolution PIV measurements, they proposed an analytical expression describing the relationship between the drag reduction and the slip velocity as $DR = U_s/U_\infty + O(\varepsilon)$, in which the first term accounts for approximately 80% of $DR$, and the second term is related to the difference of turbulent dynamics between the SHPO and smooth surfaces. Based on this theory, for the SHPO$^{\#1}$ surface which creates a significant $DR$ of 46% at $U_\infty = 0.55$ m/s, the $U_s$ is evaluated to be around 0.2 m/s if given the magnitude of $U_s/U_\infty$ equals to 80% of the total drag reduction. Other sources contributing to this drag reduction may be associated with the attenuated turbulent structures over the SHPO$^{\#1}$ surface, as evidenced by the diminished Reynolds stresses of $\langle\overline{uu}\rangle_0^+$ and $\langle\overline{vv}\rangle_0^+$ shown in Fig. 8.

## B. Scaling of drag reduction

Past numerical and experimental studies[13,36,38] indicated that the drag reduction may be correlated with the dimensionless gap between two neighboring grates, i.e., $g_0^+$. Nevertheless, based on presently measured $DR$ and the experimental data in the literature, the distribution of $DR$ against $g_0^+$ is found to be greatly scattered, as summarized in Fig. 9. For instance, given the same $f_a = 50\%$, $DR$ of SHPO$^{\#1}$ surface rises from 41% to 46% at relatively small $g_0^+$ from 0.5 to 0.8, but a further increase in $g_0^+$ to 0.8–1.3, corresponding to the SHPO$^{\#2}$ surface, leads to a drop in $DR$ to 33%–37%. Similar observations can be also made at large $f_a = 90\%$, in which the $DR$ varies from 18% to 65% in a range of $g_0^+$ from 1 to 25.[11–13] These results imply that using $f_a$, $g_0^+$, or their combination, may not be adequate to achieve a meaningful correlation between $DR$ and the surface topology.

An empirical scaling of the drag reduction is, therefore, conducted. The meniscus deformation, which has been manifested to have an important impact on drag reduction,[13,53] was usually neglected in previous investigations. Its effect is also supported by the present force balance measured $DR$ results as shown in Fig. 6. According to Eqs. (3.2)–(3.4), the meniscus deformation can be dictated by the non-dimensional curvature of air–water interface $k_c$. Through a careful analysis of present experimental data and those in the literature, we propose a relationship among $DR$, $g_0^+$, $f_a$, and $k_c$, viz.,

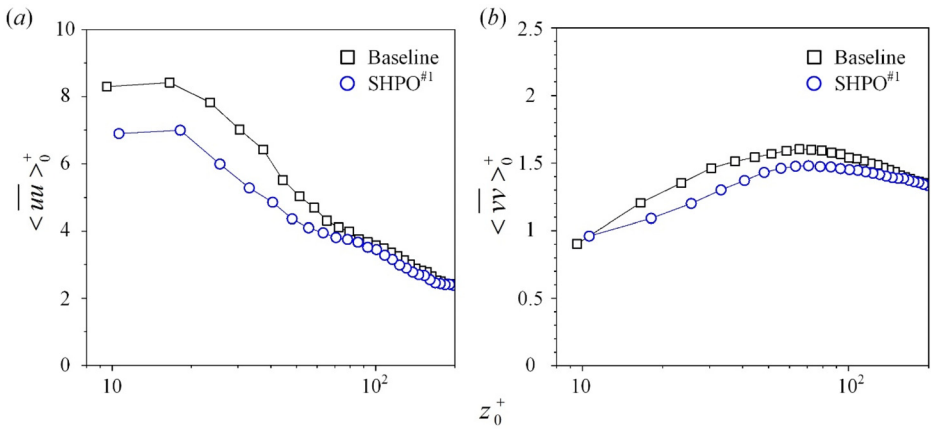


**FIG. 8.** Profiles of Reynolds stresses (a) $\langle\overline{uu}\rangle_0^+$ and (b) $\langle\overline{vv}\rangle_0^+$ over the smooth and SHPO$^{\#1}$ surfaces at $Re_L = 6.9 \times 10^6$.

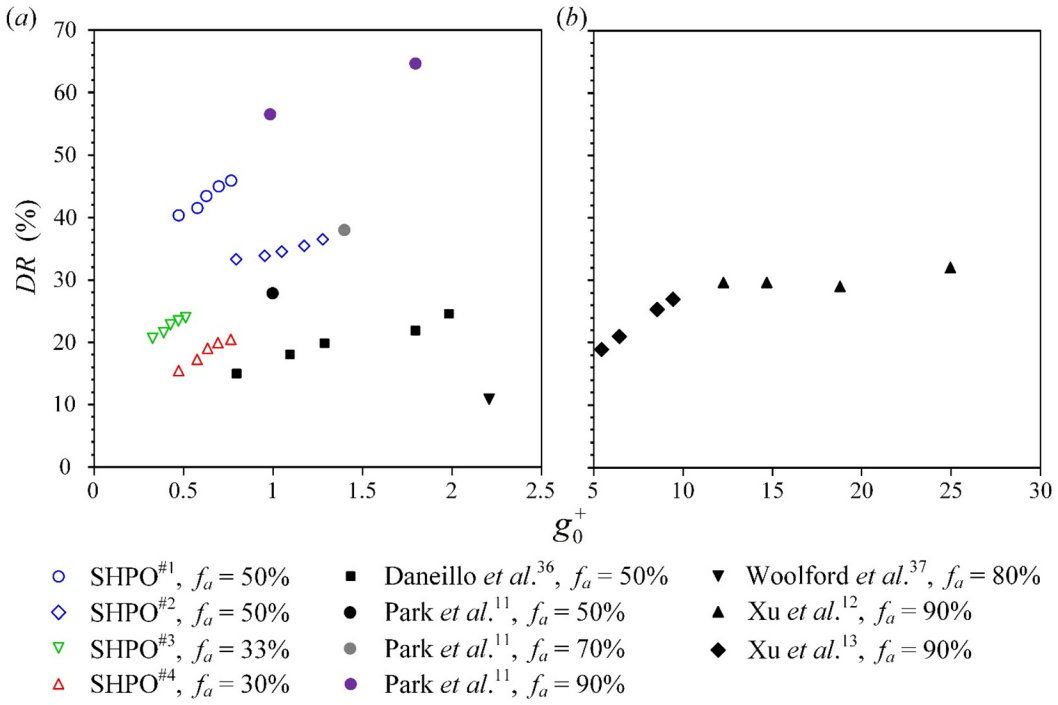


**FIG. 9.** The *DR* corresponding to $g_0^+$ in present measurements and previous experimental studies using streamwise-aligned micro-grates for (*a*) $g_0^+ < 2.5$ and (*b*) $5 < g_0^+ < 30$.

$$DR = \Theta\left(g_0^+\right)\Phi(f_a)\,\Psi(k_c), \tag{3.5}$$

where $\Theta$, $\Phi$, and $\Psi$ are functions of $g_0^+$, $f_a$, and $k_c$, respectively. Equation (3.5) considers the positive effects of $g_0^+$ and $f_a$ on *DR*, and the negative influence of the meniscus deformation, as evident in Fig. 6. After numerous trial-and-error attempts in least squares-fitting the data, $\Phi$ and $\Psi$ can be expressed in forms of $a_1 f_a^2 + a_2 f_a + a_3$ and $b_1/(k_c^2 + b_2 k_c + b_3)$, respectively. Here, $a_1 \sim a_3$ and $b_1 \sim b_3$ are coefficients. Function $\Theta$ is determined by taking above two expressions into Eq. (3.5), and we obtain a reasonably good collapse for almost all the data with least squares fit by

$$DR = \frac{3.19\, g_0^{+0.2}\left(f_a^2 + 8.91 f_a - 0.17\right)}{\left[\ln\left(g_0^{+0.43} + 1.26\right) + 0.44\right]\left(k_c^2 + 21.9 k_c + 25.5\right)}. \tag{3.6}$$

The obtained scaling law is valid for a rather wide range of $Re_{\tau 0}$ from 100 to 6000. Defining the right-hand side of Eq. (3.5) as $\xi$, a linear function $DR = \xi$ can be achieved, as shown in Fig. 10. Note that the reported *DR* of 11% by Woolford *et al.*[37] using a SHPO surface with $f_a = 80\%$ and $g = 32\,\mu$m is substantially lower than that (35%) predicted by the scaling law, which may be due to the loss of plastron during measurements. Park *et al.*'s[11] measured *DR* of 65% with $f_a = 90\%$ and $g = 90\,\mu$m is much higher than the predicted value (42%). This deviation is probably due to the relatively small size of their SHPO sample surface ($1 \times 2\,\text{cm}^2$), which may cause a size effect leading to an overestimation of drag reduction.[13].

It can be inferred from the scaling law, i.e., Eq. (3.6), that for given $f_a$ and $k_c$, *DR* is proportional to the function of $H(g_0^+) = g_0^{+0.2}/[\ln(g_0^{+0.43} + 1.26) + 0.44]$, as displayed in Fig. 11. According to Eqs. (3.3) and (3.4), $\theta_p$ and the non-dimensional maximum bending depth $h_p^* = h_p/g$ of the meniscus are both dictated by $k_c$. Therefore, a constant $k_c$ may indicate almost identical $\theta_p$ and $h_p^*$ among different menisci. Given $g_0^+ = g/\delta_{v0}$, the increase in $g_0^+$ can be realized by two approaches

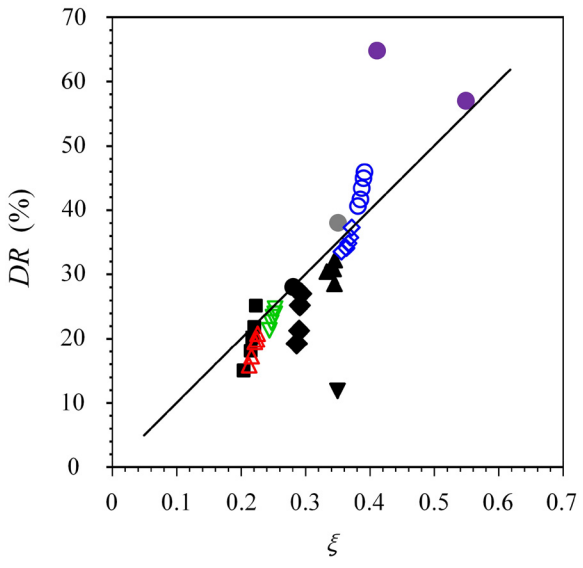


**FIG. 10.** Dependence of *DR* on the scaling factor $\xi$. The solid line is a least-square fit to the data. Symbols are as in Figs. 6 and 9.

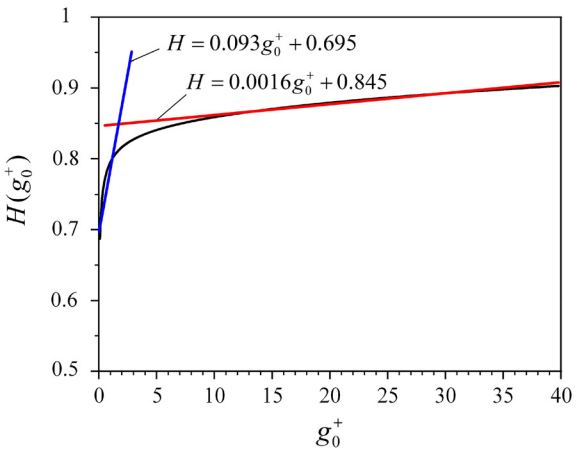


**FIG. 11.** Dependence of $H$, which is obtained from Eq. (3.6) for given $f_a$ and $k_c$, on $g_0^+$. The blue and red solid lines correspond to the linear least squares fitting to $H$ for $0.1 < g_0^+ < 2$ and $g_0^+ > 7$, respectively.

at a fixed $k_c$. One is to decrease $\delta_{v0}$ by increasing the flow velocity or Reynolds number. Another is to enlarge $g$ and, in the meantime, to reduce $\Delta P$ to retain a constant $k_c$. In both approaches, $k_c$ and the resultant $\theta_p$ and $h_p^*$ of the meniscus remain unchanged. As shown in Fig. 11, the value of $H$ is seen to climb significantly from 0.69 to 0.82 initially with $g_0^+$ rising from 0.1 to 2, but then grows slowly when $g_0^+$ is further increased, which only mildly rises to 0.9 with $g_0^+$ reaching up to 40. However, note that an overly large $g$ may lead to an unstable plastron and an easy air loss on SHPO surface,[7] which hinders its applications. Therefore, by examining the increase rate or slope of $H$ against $g_0^+$, two regions, i.e., $0.1 < g_0^+ < 2$ and $g_0^+ > 7$, can be identified. Based on the linear least-square-fitting of $H$ for $g_0^+ = 0.1$–2 and 7–40 with a fixed increment in $g_0^+$ of 0.1, the former region corresponding to high growing rates fits reasonably well to $H = 0.093\, g_0^+ + 0.695$, while the latter region with low growth rates can be fitted by $H = 0.0016\, g_0^+ + 0.845$, whose slope is only 1.7% of the former region. This result implies that, when $g_0^+$ exceeds a certain level, say $g_0^+ \approx 7$, further increasing $g_0^+$ can only marginally enhance $DR$. The understanding achieved through this scaling law could be very useful for future SHPO surface designs.

### C. Scaling of logarithmic profile on SHPO surfaces

Figure 12(a) shows $\overline{U}^+$ profiles over the smooth and SHPO surfaces at $x_0^+ = 984$, i.e., approximately $1.7\delta_B$ downstream from the leading edge of the test surface. The profile for the smooth surface is in an excellent agreement with the PIV data obtained by Ling *et al.*[21] and the DNS data from Spalart.[57] In the logarithmic layer, the $\overline{U}^+$ profile over the smooth surface collapses onto the classical logarithmic law, which is indicated by the solid line and can be expressed as

$$\overline{U_0}^+ = \frac{1}{\kappa_0}\ln z_0^+ + B_0, \tag{3.7}$$

where $\kappa_0 = 0.41$ and $B_0 = 5.0$, confirming the flow is fully turbulent. By using the Clauser method,[58] the friction velocity $u_{\tau 0}$ can be evaluated from this logarithmic relation to be about 0.0161 m/s, very close to that (0.0160 m/s) obtained directly from the skin-friction balance

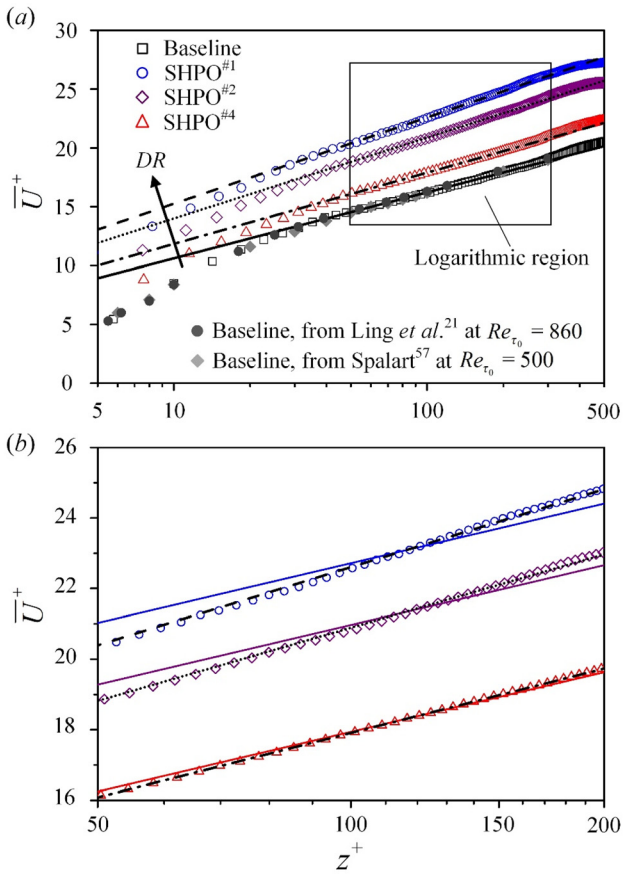


**FIG. 12.** (a) Mean streamwise velocity profiles for SHPO and baseline surfaces scaled by their own inner units. (b) Zoom-in plot at $50 < z^+ < 200$. The black solid line (—) in (a) represents the classical law of wall for the baseline surface expressed by Eq. (3.7), and the lines in (b) in blue, purple, and red colors express unchanged slopes with the classical law of wall for SHPO#1, SHPO#2, and SHPO#4 surfaces, respectively. (a) and (b) The dashed (--), dotted (···), and dashed-dotted (-·-) lines are determined by Eq. (3.8) for the three SHPO surfaces. $Re_L = 4.1 \times 10^6$. $Re_{\tau 0} = 564$.

measurements (Table III). This cross-comparison confirms the accuracy of current measurements.

When the smooth surface is replaced by the SHPO surfaces, it is found that the profiles are shifted upwards, and the extent of shift rises with the increase in $DR$. Also, the slope of the logarithmic-layer velocity profiles increases with increasing $DR$, as clearly revealed in the zoomed-in plot in Fig. 12(b).

As shown in Fig. 13, the measured $(d\overline{U}/dz)_0^+$ profiles over the smooth and SHPO surfaces collapses in the outer layer at $z_0^+ > 50$. Similar observations have also been made in Ling *et al.*'s[21] experimental study over randomly textured SHPO surfaces. They observed based on high-resolution PIV measurements that $(\mu d\overline{U}/dz)_0^+$ retained nearly unchanged when replacing the smooth surface with the drag-reducing SHPO surfaces at $z_0^+ = 50$–400. This indicates that the outer layer has not yet been affected by the change in velocity scale near the SHPO surface. In other words, the outer layer may not have reached the equilibrium condition. In this case, when re-deriving Eq. (3.7) for

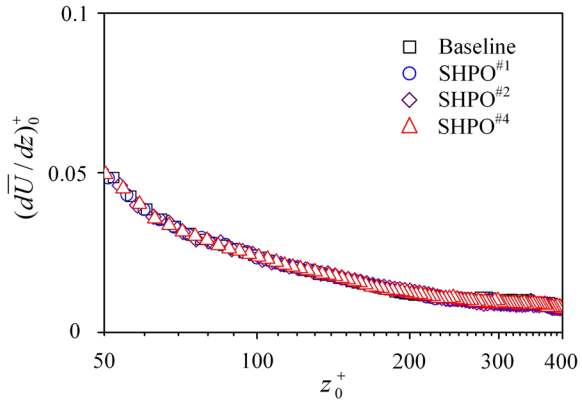


**FIG. 13.** Profiles of velocity gradient $(d\overline{U}/dz)_0^+$ over the smooth and SHPO surfaces at $Re_L = 4.1 \times 10^6$.

TBL over SHPO surfaces, if the $\overline{U}$ profile in the outer layer is normalized using $u_{\tau 0}$ (i.e., the corresponding friction velocity over a smooth surface) instead of $u_\tau$ (i.e., the actual friction velocity), a modified logarithmic relation can be obtained as (see the Appendix for detailed derivation)

$$\overline{U}^+ = \frac{1}{\kappa_0\sqrt{1-DR}}\ln z^+ + B(DR), \tag{3.8}$$

where $B$ is an additive parameter depending on $DR$. This equation clearly indicates that any drag reduction (note $0 < DR < 1$) will result in an increase in the slope of velocity profile in the logarithmic layer. The larger the $DR$, the steeper the slope, which is consistent with our observations. Furthermore, as illustrated in Fig. 12(b), the dashed, dotted, and dashed-dotted lines representing Eq. (3.8) for SHPO#1, SHPO#2, and SHPO#4 surfaces, respectively, agree well with the measured velocities, with the RMS errors of the fitting being less than 0.05, which are at least five times smaller than those evaluated with the unchanged slope [represented by solid lines in Fig. 12(b)]. Similar results have also been obtained for the SHPO#3 surface but not included in this figure, whose logarithmic layer profile can also be depicted by Eq. (3.8).

The proposed new correlation between the velocity profile slope in the logarithmic layer over SHPO surfaces and the produced drag reduction, i.e., Eq. (3.8), can also be verified by existing experimental data reported in previous studies,[21,23,59] as shown in Fig. 14. Two datasets are obtained from Ling *et al.*'s[21] PIV results for two SHPO surfaces with surface roughness $k^+$ of 0.43 and 0.89, producing $DR = 12\%$ and 27%, respectively, as well as for the smooth surface, at $Re_\tau \approx 800$ (their Figs. 5 and 11). One dataset is from Rowin and Ghaemi's[23] PIV measurements for a coated SHPO surface with $k^+ = 0.28$, creating $DR = 36\%$ at $Re_\tau \approx 800$ (their Fig. 10). One more set of data is from Hu *et al.*'s[59] hot-film anemometer measurements over a SHPO surface ($k^+ = 0.04$), which led to $DR = 14\%$ at $Re_\tau \approx 700$ (their Fig. 5). The theoretical predictions based on Eq. (3.8) for these cases with $DR = 36\%$, 27%, 14%, and 12% are plotted with lines. It is seen that all the datasets agree well with the theoretical predictions for the logarithmic layer.

Figure 15 presents the variation of $B$ in Eq. (3.8), which is determined by fitting the $DR$-induced logarithmic profile for the SHPO surfaces. It is interesting to note that $B$ displays an approximately linear relationship with $DR$. The data fit well with the equation as

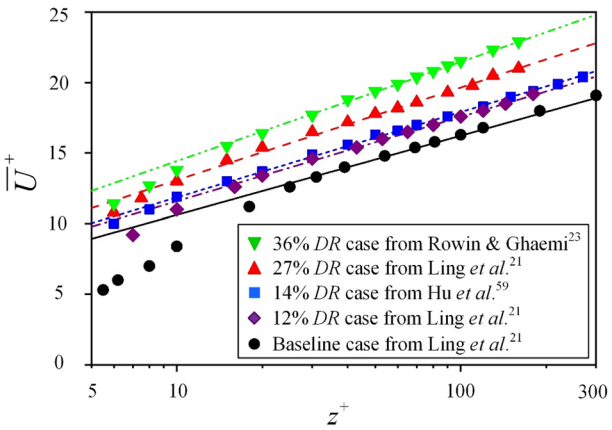


**FIG. 14.** Mean streamwise velocity profiles obtained from Ling *et al.*,[16] Rowin and Ghaemi,[18] and Hu *et al.*[54] experimental data of the baseline and SHPO surfaces and scaled by their own inner units. The solid line (—) is as in Fig. 12. The dashed (- -), dashed-dotted (-·-), dotted (···), and dashed-dotted-dotted (-··-) lines are determined by Eq. (3.8), in which the line colors: green for the case of $DR$ of 36%, red, 27%; blue, 14%; purple, 12%.

$$B(DR) = B_0 + k_D DR \tag{3.9}$$

with $K_D = 6.6$. Note that the values of $B$ are not provided in Ling *et al.*,[21] Rowin and Ghaemi,[23] or Hu *et al.*[59] Instead, they are calculated based on their logarithmic profiles data, which are found to be about 5.6, 5.8, 6.6, and 7.5 for the $DR$ cases of 12%, 14%, 27%, and 36%, respectively. The deviations of these $B$ values from those (5.8, 5.9, 6.8, and 7.4) predicted by Eq. (3.9) are relatively small, less than 4%.

It is worth commenting on the range of validity of the proposed theory. The present logarithmic profile scaling in TBL over the SHPO surface is based on the assumption that only the inner part of the boundary layer is affected by wall manipulation while the outer part has not reached a new equilibrium. In contrast, if the SHPO surface is

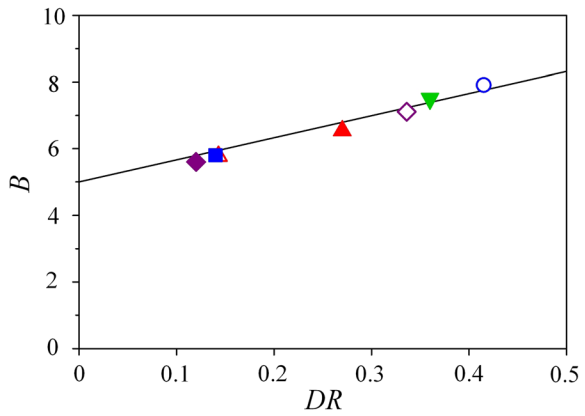


**FIG. 15.** Dependence of $B$ on $DR$. Symbols are as Figs. 12 and 14. The solid line is calculated by Eq. (3.9).

sufficiently long so that the outer layer can eventually adjust to the wall manipulation and reach the new equilibrium, the outer layer may scale with the actual friction velocity. In this case, the logarithmic scaling may restore to the classical form with the slope of $1/\kappa_0$. Nevertheless, there is nearly no numerical or experimental documentation on how far downstream in TBL over a SHPO surface could the outer layer adjust to the new equilibrium, and the resultant modification of the logarithmic scaling law remains unknown.

## IV. CONCLUSIONS

We developed a high-resolution skin-friction balance to measure in a water tunnel the drag reduction of streamwise-micro-grated SHPO surfaces in TBL. Four SHPO surfaces with different micro-grate sizes were investigated, all exhibiting an increase in *DR* with increasing $Re_L$. Significant *DR* from 41% to 46% was obtained for the SHPO$^{\#1}$ surface with $f_a = 50\%$ at $Re_L = (4.1\text{–}6.9) \times 10^5$. However, with the same $f_a$ and $Re_L$ but a larger deformation of meniscus on the gap between grates, the *DR* of the SHPO$^{\#2}$ surface was decreased to 33%–37%, which confirms that the meniscus deformation has an important impact on drag reduction as pointed out by previous numerical studies. The SHPO$^{\#3}$ and SHPO$^{\#4}$ surfaces led to lower *DR* (20%–24%), which is due to smaller $f_a$ (33% and 30%, respectively). Moreover, for each SHPO surface, the *DR* is observed to monotonically increase with ascending $g_0^+$, indicating a positive effect of $g_0^+$ on the drag reduction.

Empirical scaling of drag reduction is conducted with a view to achieving a correlation between *DR* and surface topology. With the non-dimensional meniscus curvature $k_c$ included, *DR* can be predicted reasonably well by a function of $k_c$, $f_a$, and $g_0^+$, as expressed by Eq. (3.6), with which all the present and previous experimental data collapse well, conciliating the widely scattered *DR* data in the literature. Moreover, it is found based on this scaling law that, given fixed $k_c$ and $f_a$, the growth rate or slope of *DR* against $g_0^+$ at $g_0^+ < 2$ is approximately 58 times higher than that when $g_0^+$ exceeds 7. In view of the fact that a large $g$ may lead to unstable plastrons, this finding may provide a valuable guidance for the design of effective SHPO surface topology in real-world applications.

Furthermore, a theoretical expression predicting the slope and the up-shifting level of the logarithmic profile for SHPO surfaces was proposed. This logarithmic scaling analysis was conducted under the condition that the outer layer of TBL has not reached a new equilibrium when subjected to the SHPO surface manipulation, which is a common occurrence in laboratory experiments in view of the limited length of manufactured SHPO surface samples. Therefore, by assuming that the outer layer has not been affected by the SHPO surface condition and, hence, is still governed by the friction velocity on the smooth surface, the slope of logarithmic profile is found to be modified to $1/(\kappa_0\sqrt{1-DR})$, and the up-shifting level $B$ grows almost linearly with the magnitude of *DR*, as described by Eqs. (3.8) and (3.9), respectively. This is supported not only by our own PIV data but also by existing experimental data from other groups. These findings may inspire researchers in the field and provide them with a new perspective to examine their measured or simulated velocity and *DR* data.

## ACKNOWLEDGMENTS

The authors wish to acknowledge support given to them from the National Natural Science Foundation of China (NSFC) through Grant Nos. 12272114 and 91952107 and from the Research Grants Council of Shenzhen Government through Grant No. CB11409006. The work described in this paper was supported by a grant from the General Research Fund from the Research Grants Council of the Hong Kong Special Administrative Region (Project No. 15221322); the funding support to the State Key Laboratories in Hong Kong from the Innovation and Technology Commission (ITC) of the Government of the Hong Kong Special Administrative Region (HKSAR), China, is also greatly acknowledged. The authors would also like to express their sincere thanks to the Research and Innovation Office of The Hong Kong Polytechnic University for the financial support.

## AUTHOR DECLARATIONS

### Conflict of Interest

The authors have no conflicts to disclose.

### Author Contributions

**Bingfu Zhang:** Conceptualization (equal); Data curation (equal); Formal analysis (equal); Investigation (equal); Methodology (equal); Writing – original draft (equal); Writing – review & editing (equal). **Feng Guo:** Data curation (supporting); Formal analysis (supporting); Investigation (supporting); Methodology (supporting); Writing – original draft (supporting); Writing – review & editing (supporting). **Suet To:** Conceptualization (supporting); Investigation (supporting); Methodology (supporting); Project administration (supporting); Resources (supporting); Writing – original draft (supporting); Writing – review & editing (supporting). **Hui Tang:** Conceptualization (equal); Data curation (equal); Formal analysis (equal); Investigation (equal); Methodology (equal); Project administration (equal); Resources (equal); Writing – original draft (equal); Writing – review & editing (equal).

## DATA AVAILABILITY

The data that support the findings of this study are available from the corresponding authors upon reasonable request.

## APPENDIX: LOGARITHMIC SCALING OF TBL ON SHPO SURFACE

The classical scaling of TBL along a flat surface describes the mean velocity profile $\overline{U}$ using two layers, i.e., inner and outer layers. Normally, the inner and outer layers are located at $z/\delta_B < 0.2$ and $z/\delta_v > 50$, respectively, which have an overlap region.[60] In this overlap region, the dependence of $\overline{U}^+$ on $z^+$ is described by a logarithmic relationship, which can be determined by matching the velocity gradient in the inner and outer layers.[61] Specifically, since the flow in the inner layer is characterized by inner viscous length $\delta_v$, the $\overline{U}^+$ depends on $z^+$, i.e.,

$$\overline{U}^+ = F(z^+), \tag{A1}$$

where $F$ is a function of $z^+$. Hence, the velocity gradient in this layer can be evaluated by

$$\frac{d\overline{U}}{dz} = \frac{dF(z^+)}{dz^+}\frac{u_\tau}{\delta_v} = \frac{dF(z^+)}{dz^+}\frac{u_\tau^2}{\upsilon}. \tag{A2}$$

On the other hand, the flow in the outer layer is characterized by the boundary layer thickness $\delta_B$ where the viscous effect is negligible.[62] Hence, the $\overline{U}^+$ depends on $\zeta = z/\delta_B$ instead of $z^+$, i.e.,

$$\overline{U}^+ = G(\zeta), \tag{A3}$$

where $G$ is a function of a normalized variable $\zeta$. The velocity gradient in this layer is then

$$\frac{d\overline{U}}{dz} = \frac{dG(\zeta)}{d\zeta}\frac{u_\tau}{\delta_B}. \tag{A4}$$

By matching the two velocity gradients expressed in Eqs. (A2) and (A4), we can obtain the classical logarithmic law for the overlap layer as

$$\overline{U}^+ = \frac{1}{\kappa}\ln z^+ + B, \tag{A5}$$

which, if applied to a smooth surface, becomes Eq. (3.7) in this paper. Note that $\kappa$ and $B$ vary for different surfaces such as in the present study.

To explicitly incorporate the effect of drag reduction into the evaluation for the SHPO surfaces, we nondimensionalize $\overline{U}$ in Eq. (A4) using a reference velocity $u_{\tau 0}$, i.e., the viscous velocity over the smooth surface under the same flow conditions, instead of the actual velocity $u_\tau$

$$\frac{d\overline{U}}{dz} = \frac{dG_0(\zeta)}{d\zeta}\frac{u_{\tau 0}}{\delta_B}, \tag{A6}$$

where $G_0$ is another function of $\zeta$. In the non-equilibrium state, in which the outer layer has not been impacted by the change of velocity scale on the SHPO surface, the new nondimensional velocity gradient, i.e., $dG_0/d\zeta$, remains the same when surface changes. This is supported by our experimental observation where the measured $d\overline{U}/dz$ profiles over all the surfaces, including the smooth and SHPO surfaces, collapse when $z$ is sufficiently large, as reflected in Fig. 13.

Thus, matching the two velocity gradients expressed in Eqs. (A2) and (A6) gives

$$\frac{dF(z^+)}{dz^+}\frac{u_\tau^2}{\upsilon} = \frac{dG_0(\zeta)}{d\zeta}\frac{u_{\tau 0}}{\delta_B}. \tag{A7}$$

Multiplying both sides of Eq. (A7) by $z$ and re-arranging the terms, we obtain

$$z^+\frac{dF(z^+)}{dz^+}\frac{u_\tau}{u_{\tau 0}} = \zeta\frac{dG_0(\zeta)}{d\zeta}. \tag{A8}$$

Note that the wall shear stress $\tau_w$ is related to $u_\tau$ and also to friction drag coefficient $C_f$

$$\tau_w = \rho u_\tau^2 = C_f \rho U_\infty^2/2. \tag{A9}$$

Hence,

$$\frac{u_\tau}{u_{\tau 0}} = \sqrt{\frac{C_f}{C_{f0}}} = \sqrt{1 - DR}. \tag{A10}$$

As such, Eq. (A8) can explicitly include a quantity related to drag reduction

$$z^+\frac{dF(z^+)}{dz^+}\sqrt{1 - DR} = \zeta\frac{dG_0(\zeta)}{d\zeta}. \tag{A11}$$

The two sides of Eq. (A11) depend on different variables. By applying the separation of variables concept and by noting that, when $DR = 0$, the resulting expression should recover to the logarithmic law of a smooth surface, the left side of Eq. (A11) becomes

$$z^+\frac{d\overline{U}^+}{dz^+} = \frac{1}{\kappa_0\sqrt{1 - DR}}. \tag{A12}$$

Integrating this equation yields Eq. (3.8).

## REFERENCES


[1] B. R. Zheng, D. L. Lin, S. J. Qi, Y. Z. Hu, Y. Z. Jin, Q. L. Chen, D. L. Bian, and R. H. Yan, "Turbulent skin-friction drag reduction by annular dielectric barrier discharge plasma actuator," Phys. Fluids **35**, 125129 (2023).
[2] X. Zhang, C. W. Wong, X. Q. Cheng, and Y. Zhou, "Dependence of skin-friction reduction on the geometric parameters of blowing jet array," Phys. Fluids **34**, 105125 (2022).
[3] K. U. Kempaiah and F. Scarano, "Feature-based analysis of a turbulent boundary layer under spanwise wall oscillation," Phys. Fluids **34**, 115152 (2022).
[4] X. T. Cui, N. Jiang, X. B. Zheng, and Z. Q. Tang, "Active control of multiscale features in wall-bounded turbulence," Acta Mech. Sin. **36**, 12–21 (2020).
[5] T. F. Zheng, J. B. Liu, L. G. Qin, S. Lu, F. J. Mawignon, Z. Y. Ma, L. X. Hao, Y. H. Wu, D. An, and G. N. Dong, "Effect of dolphin-inspired transverse wave microgrooves on drag reduction in turbulence," Phys. Fluids **36**, 015157 (2024).
[6] B. Liu and Y. M. Zhang, "A numerical study on the natural transition locations in the flat-plate boundary layers on superhydrophobic surfaces," Phys. Fluids **32**, 124103 (2020).
[7] H. Park, C. H. Choi, and C. J. Kim, "Superhydrophobic drag reduction in turbulent flows: A critical review," Exp. Fluids **62**, 229 (2021).
[8] L. J. Qian, C. Huang, L. Lv, Q. F. Fu, and C. Fu, "Dynamic behavior of droplets impacting cylindrical superhydrophobic surfaces with different structures," Phys. Fluids **35**, 023331 (2023).
[9] H. Rahmani, H. Kumar, J. Greener, and S. N. Taghavi, "Yield stress fluid flows in superhydrophobic channels: From creeping to inertial regime," Phys. Fluids **35**, 083107 (2023).
[10] U. Kim, H. Kim, and J.-H. Kim, "Deposition of micro/macroscale water droplets on grooved hydrophobic surfaces," Phys. Fluids **34**, 112106 (2022).
[11] H. Park, G. Y. Sun, and C. J. Kim, "Superhydrophobic turbulent drag reduction as a function of surface grating parameters," J. Fluid Mech. **747**, 722–734 (2014).
[12] M. Xu, A. Grabowski, N. Yu, G. Kerezyte, J. W. Lee, B. R. Pfeifer, and C. J. Kim, "Superhydrophobic drag reduction for turbulent flows in open water," Phys. Rev. Appl. **13**, 034056 (2020).
[13] M. Xu, N. Yu, J. Kim, and C. J. Kim, "Superhydrophobic drag reduction in high-speed towing tank," J. Fluid Mech. **908**, A6 (2021).
[14] M. B. Martell, J. P. Rothstein, and J. B. Perot, "An analysis of superhydrophobic turbulent drag reduction mechanisms using direct numerical simulation," Phys. Fluids **22**, 065102 (2010).
[15] J. Seo and A. Mani, "On the scaling of the slip velocity in turbulent floes over superhydrophobic surfaces," Phys. Fluids **28**, 025110 (2016).
[16] Y. Liu, M. Y. Wu, Z. Y. Zhang, K. Y. Luo, J. Z. Lu, L. Q. Lin, K. Xu, H. Zhu, B. Wang, W. N. Lei, and Y. Q. Fu, "Fabrication of wear-resistant and superhydrophobic aluminum alloy surface by laser-chemical hybrid methods," Phys. Fluids **35**, 052108 (2023).
[17] P. Dey, S. K. Saha, and S. Chakraborty, "Microgroove geometry dictates slippery hydrodynamics on superhydrophobic substrates," Phys. Fluids **30**, 122007 (2018).
[18] Q. D. Chen, J. Duan, Z. B. Hou, G. X. Hou, and L. M. Deng, "Effect of the surface pattern on the drag property of the superhydrophobic surface," Phys. Fluids **34**, 114113 (2022).
[19] J. G. Hu and Z. H. Yao, "Drag reduction of turbulent boundary layer over sawtooth riblet surface with superhydrophobic coat," Phys. Fluids **35**, 015104 (2023).

[20]B. V. Hokmabad and S. Ghaemi, "Turbulent flow over wetted and non-wetted superhydrophobic counterparts with random structure," Phys. Fluids **28**, 015112 (2016).
[21]H. J. Ling, S. Srinivasan, K. Golovin, G. H. McKinley, A. Tuteja, and J. Katz, "High-resolution velocity measurement in the inner part of turbulent boundary layers over super-hydrophobic surfaces," J. Fluid Mech. **801**, 670–703 (2016).
[22]J. W. Gose, K. Golovin, M. Boban, J. M. Mabry, A. Tuteja, M. Perlin, and S. L. Ceccio, "Characterization of superhydrophobic surfaces for drag reduction in turbulent flow," J. Fluid Mech. **845**, 560–580 (2018).
[23]W. A. Rowin and S. Ghaemi, "Effect of Reynolds number on turbulent channel flow over a superhydrophobic surface," Phys. Fluids **32**, 075105 (2020).
[24]E. Taghvaei, A. Moosavi, A. Nouri-Borujerdi, M. A. Daeian, and S. Vafaeinejad, "Superhydrophobic surfaces with a dual-layer micro- and nanoparticle coating for drag reduction," Energy **125**, 1–10 (2017).
[25]W. Choi, M. Kang, J. Y. Park, H. E. Jeong, and S. J. Lee, "Enhanced air stability of superhydrophobic surfaces with flexible overhangs of re-entrant structures," Phys. Fluids **33**, 022001 (2021).
[26]M. Zhu, J. Huang, Q. Zhou, and Z. H. Yao, "Study on the evolution and stability of gas–liquid interfaces based on composite structures on the sidewall surface of a microchannel," Phys. Fluids **35**, 082005 (2023).
[27]C. Lee and C. J. Kim, "Underwater restoration and retention of gases on superhydrophobic surfaces for drag reduction," Phys. Rev. Lett. **106**, 014502 (2011).
[28]D. Panchanathan, A. Rajappan, K. K. Varanasi, and G. H. McKinley, "Plastron regeneration on submerged superhydrophobic surfaces using *in situ* gas generation by chemical reaction," ACS Appl. Mater. Interfaces **10**, 33684–33692 (2018).
[29]P. Du, J. Wen, Z. Z. Zhang, D. Song, A. Ouahsine, and H. B. Hu, "Maintenance of air layer and drag reduction on superhydrophobic surface," J. Ocean Eng. **130**, 328–335 (2017).
[30]H. Sung, H. Choi, C. Ha, C. Lee, and H. Park, "Plastron replenishment on superhydrophobic surfaces using bubble injection," Phys. Fluids **34**, 103323 (2022).
[31]W. Cho, S. Heo, and S. J. Lee, "Effects of surface air injection on the air stability of superhydrophobic surface under partial replenishment of plastron," Phys. Fluids **34**, 122115 (2022).
[32]C. Lee, C. H. Choi, and C. J. Kim, "Superhydrophobic drag reduction in laminar flows: A critical review," Exp. Fluids **57**, 176 (2016).
[33]H. Ems, A. Tsubaki, B. Sukup, S. Nejati, D. Alexander, C. Zuhlke, and G. Gogos, "Drag reduction in minichannel laminar flow past superhydrophobic surfaces," Phys. Fluids **33**, 123608 (2021).
[34]A. Rastegari and R. Akhavan, "On the mechanism of turbulent drag reduction with superhydrophobic surfaces," J. Fluid Mech. **773**, R4 (2015).
[35]H. Y. Li, S. S. Ji, X. K. Tan, Z. X. Li, Y. L. Xiang, P. Y. Lv, and H. L. Duan, "Effect of Reynolds number on drag reduction in turbulent boundary layer over liquid-gas interface," Phys. Fluids **32**, 122111 (2020).
[36]R. J. Daniello, N. E. Waterhouse, and J. P. Rothstein, "Drag reduction in turbulent flows over superhydrophobic surfaces," Phys. Fluids **21**, 085103 (2009).
[37]B. Woolford, J. Prince, D. Maynes, and B. W. Webb, "Particle image velocimetry characterization of turbulent channel flow with rib patterned superhydrophobic walls," Phys Fluids **21**, 085106 (2009).
[38]H. Park, H. Park, and J. Kim, "A numerical study of the effects of superhydrophobic surface on skin-friction drag in turbulent drag in turbulent channel flow," Phys. Fluids **25**, 110815 (2013).
[39]M. A. Samaha and M. Gad-el-Hak, "Slippery surfaces: A decade of progress," Phys. Fluids **33**, 071301 (2021).
[40]J. X. Zhang, H. P. Tian, Z. H. Yao, P. F. Hao, and N. Jiang, "Mechanisms of drag reduction of superhydrophobic surfaces in a turbulent boundary layer flow," Exp. Fluids **56**, 179 (2015).
[41]H. P. Tian, J. X. Zhang, N. Jiang, and Z. H. Yao, "Effect of hierarchical structured superhydrophobic surfaces on coherent structures in turbulent channel flow," Exp. Therm. Fluid Sci. **69**, 27–37 (2015).
[42]P. A. Krogstad and V. Efros, "Rough wall skin friction measurements using a high resolution surface balance," Int. J. Heat Fluid Flow **31**, 429–433 (2010).
[43]D. Li, Y. Q. Liu, K. Luo, and J. R. Fan, "An integral method to determine mean skin friction in turbulent boundary layers," Phys. Fluids **35**, 035127 (2023).
[44]B. F. Zhang, K. Liu, Y. Zhou, S. To, and J. Y. Tu, "Active drag reduction of a high-drag Ahmed body based on steady blowing," J. Fluid Mech. **856**, 351–396 (2018).
[45]B. F. Zhang, D. W. Fan, and Y. Zhou, "Artificial intelligence control of a low-drag Ahmed body using distributed jet arrays," J. Fluid Mech. **963**, A3 (2023).
[46]X. Wen, H. Tang, and F. Duan, "Vortex dynamics of in-line twin synthetic jets in a laminar boundary layer," Phys. Fluids **27**, 083601 (2015).
[47]A. Sciacchitano, B. Wieneke, and F. Scarano, "PIV uncertainty quantification by image matching," Meas. Sci. Technol. **24**, 045302 (2013).
[48]B. F. Zhang, Y. Zhou, and S. To, "Unsteady flow structures around a high-drag Ahmed body," J. Fluid Mech. **777**, 291–326 (2015b).
[49]F. M. White, *Viscous Fluid Flow*, 2nd ed. (McGraw Hill Inc., New York, 1991).
[50]R. A. Bidkar, L. Leblanc, A. J. Kulkarni, V. Bahadur, S. L. Ceccio, and M. Perlin, "Skin-friction drag reduction in the turbulent regime using random-textured hydrophobic surfaces," Phys. Fluids **26**, 085108 (2014).
[51]C. Henoch, T. N. Krupenkin, P. Kolodner, J. A. Taylor, M. S. Hodes, A. M. Lyons, C. Peguero, and K. Breuer, "Turbulent drag reduction using superhydrophobic surfaces," AIAA paper No. 2006-3192, 2006.
[52]E. Aljallis, M. A. Sarshar, R. Datla, V. Sikka, A. Jones, and C. H. Choi, "Experimental study of skin friction drag reduction on superhydrophobic flat plates in high Reynolds number boundary layer flow," Phys. Fluids **25**, 025103 (2013).
[53]A. Rastegari and R. Akhavan, "The common mechanism of turbulent skin-friction drag reduction with superhydrophobic longitudinal microgrooves and riblets," J. Fluid Mech. **838**, 68–104 (2018).
[54]P. Dey, S. K. Saha, and S. Chakraborty, "Air-water meniscus shape in superhydrophobic triangular microgroove is dictated by a critical pressure under dynamic conditions," Phys. Fluids **31**, 102004 (2019).
[55]J. Yao and C. J. Teo, "Effect of the liquid–gas interface curvature for a superhydrophobic surface with longitudinal grooves in turbulent flows," Phys Fluids **33**, 075116 (2021).
[56]M. Sbragaglia and A. Prosperetti, "A note on the effective slip properties for microchannel flows with ultrahydrophobic surfaces," Phys. Fluids **19**, 043603 (2007).
[57]P. R. Spalart, "Direct simulation of a turbulent boundary layer up to $Re_\theta = 1410$," J. Fluid Mech. **187**, 61–98 (1988).
[58]T. Wei, R. Schmidt, and P. McMurtry, "Comment on the Clauser chart method for determining the friction velocity," Exp. Fluids **38**, 695–699 (2005).
[59]H. B. Hu, P. Du, F. Zhou, D. Song, and Y. Wu, "Effect of hydrophobicity on turbulent boundary layer under water," Exp. Therm. Fluid Sci. **60**, 148–156 (2015).
[60]M. Perlin, D. R. Dowling, and S. L. Ceccio, "Freeman scholar review: Passive and active skin-friction drag reduction in turbulent boundary layers," J. Fluids Eng. **138**, 091104 (2016).
[61]A. G. Gungor, Y. Maciel, M. P. Simens, and J. Soria, "Scaling and statistics of large-defect adverse pressure gradient turbulent boundary layers," Int. J. Heat Fluid Flow **59**, 109–124 (2016).
[62]S. B. Pope, *Turbulent Flows* (Cambridge University Press, 2001).